Photonics-Based Simultaneous Angle of Arrival and Frequency Measurement System With Multiple-Target Detection Capability

Yue Yang, Cong Ma, Beichen Fan, Xiangchuan Wang, Fangzheng Zhang, *Senior Member, IEEE*, Yu Xiang, and Shilong Pan, *Senior Member, IEEE, Fellow, OSA*

***Abstract*—A photonics-based system for simultaneous angle of arrival (AOA) and frequency measurement is proposed and demonstrated. In the proposed system, an acousto-optic modulator (AOM) based optical frequency shift loop (OFSL) is used to generate an optical frequency-stepped local oscillator (LO). After balanced in-phase and quadrature (I/Q) down-conversion with the frequency-stepped LO, the frequency to be measured is obtained. Thanks to the balanced I/Q down-conversion, the image frequencies and undesired frequency-mixing components can be suppressed, making the system have better adaptability to multiple-target scenarios. In addition, the AOA from different RF sources can also be estimated based on the Van Cittert–Zernike theorem, even if the working bands of these targets overlap with each other. In the proof-of-concept experiment, the measurement of multiple targets with different frequencies is achieved by frequency detection with 0.179 MHz resolution. Moreover, incoherent microwave sources at the same frequency band can also be distinguished in the angular direction, achieving the capacity of simultaneous frequency and AOA measurement of multiple-target.**

***Index Terms*—Angle of arrival, frequency measurement, microwave photonics, passive detection.**

I. Introduction

ANGLE of arrival (AOA) can be used to determine the direction of the target, which is of critical importance in modern radar, communication, and electronic warfare systems [1]–[3]. Generally, passive AOA measurement, mainly used for detecting radio frequency (RF) sources, is achieved by comparing the phase or time delay difference between the RF signals collected by multiple antenna elements in an array. However, with the increasing demand for high-resolution detection and high-speed wireless communication, the RF systems must have the ability to process signals over a large frequency range, sometimes up to tens of gigahertz, which is a great challenge for traditional electronic technology.

RF systems based on microwave photonics (MWP) have the capability of generating, transmitting, and processing RF signals with large bandwidth [4]–[7]. By up-converting the RF signals to the optical domain, the advantages of photonic technologies including large operation bandwidth, ultra-low transmission loss, and electromagnetic interference immunity can be achieved [8]–[14]. Recently, various AOA measurement methods based on MWP technologies have been proposed [15]–[25]. A simple technique to measure the AOA of a broadband signal with an optical beamformer array is proposed in [15], where the AOA is obtained from the free-spectral range (FSR) of the system frequency response. In [16], the AOA is estimated by measuring the optical power. By applying two cascaded modulators, the phase difference of two antennas is converted to the optical power at carrier wavelength. Several similar power measurement based AOA estimation methods such as measuring the optical sideband power [17], the output microwave signal power [18], or DC voltage [19] are also proposed. However, a calibration procedure should be performed before the AOA estimation to avoid the influence of incoming signal power. To address this, a photonics-based system combining a polarization-division-multiplexed dual-drive Mach-Zehnder modulator (PDM-DMZM) and an optical notch filter is presented [20]. By measuring the ratio of two DC voltages generated by low-speed photodetectors, AOA estimation can be realized independent of the input signal power. Besides, a phase scanning based method is proposed to achieve AOA measurement through scanning the phase of optical sideband from 0 to 2π [21]. But due to the bandwidth limitation of optical filters, the two systems mentioned above can hardly measure the low-frequency signals. Another approach utilizing the frequency to identify the AOA is presented in [22]. Although the measurement accuracy is relatively high, it can only detect the AOA of linear frequency modulated (LFM) signals, leading to limited application scenarios. Among the above-mentioned MWP-based AOA measurement methods, it is not easy to achieve multiple-target detection. A tunable photonic mixer based method for measuring the AOA of multiple signals is proposed with prior information of the signal frequency and only signals with different frequencies can be detected

Manuscript received March 31, 2021; revised June 1, 2021; accepted June 4, 2021. Date of publication June 8, 2021; date of current version December 16, 2021. This work was supported in part by the National Natural Science Foundation of China under Grants 61871214, 62075095, 61527820, and 11804159, in part by Natural Science Foundation of Jiangsu Province under Grant BK20180066, in part by Young Elite Scientists Sponsorship Program by CAST under Grant 2018QNRC001, and in part by Jiangsu Provincial "333" Project under Grant BRA2018042. *(Corresponding authors: Fangzheng Zhang; Shilong Pan).*

The authors are with the Key Laboratory of Radar Imaging and Microwave Photonics, Ministry of Education, Nanjing University of Aeronautics and Astronautics, Nanjing 210016, China (e-mail: zhangfangzheng@nuaa.edu.cn; pans@ieee.org).

Color versions of one or more figures in this article are available at https://doi.org/10.1109/JLT.2021.3087526.

Digital Object Identifier 10.1109/JLT.2021.3087526

0733-8724 © 2021 IEEE. Personal use is permitted, but republication/redistribution requires IEEE permission.
See https://www.ieee.org/publications/rights/index.html for more information.

Authorized licensed use limited to: NANJING UNIVERSITY OF AERONAUTICS AND ASTRONAUTICS. Downloaded on June 06,2022 at 04:05:33 UTC from IEEE Xplore. Restrictions apply.

[23]. However, the frequencies of non-cooperation microwave sources are also unknown as well as the AOA in practice. Therefore, simultaneous AOA and frequency measurement is highly required in practical applications.

A coherent optical processing method based on space optics is presented, where RF signals from different directions can be distinguished in real-time through compact lens-based optics [26]–[28]. Meanwhile, the signal frequency can also be resolved through a temporal aperture composed of fibers with different lengths. Although this method can realize frequency and AOA detection for multiple-target, the frequency resolution is only a few hundred megahertz, which is far from actual demand.

Recently, we have proposed and demonstrated a photonics-based simultaneous AOA and frequency measurement system having the capability of multiple-target detection [29]. The proposed AOA and frequency measurement system has several advantages compared to previous methods. Firstly, multiple-target detection, especially when the targets' working frequency bands overlap with each other is achieved through the array signal processing algorithm based on Van Cittert–Zernike theorem. Secondly, frequency measurement without image-frequency interference and undesired frequency-mixing components is realized at the same time through optical time-division channelized balanced in-phase and quadrature (I/Q) down-conversion. Thirdly, the proposed system is able to characterize the intensity of different targets as well as the AOA and frequency, so it has the potential to be further extended to realize 2-D imaging [30] and even 3-D k-space imaging [26]. However, only some brief theoretical derivation as well as experiment results are included in [29], which cannot fully prove the performance of the system.

In this paper, a comprehensive theoretical analysis of the proposed photonics-based simultaneous AOA and frequency measurement system is performed while proof-of-concept experiments are also carried out. In Section II, the principle of the proposed system is introduced in detail. In Section III, frequency and AOA measurement experiments for single-target and dual-target detection are investigated separately. The benefits brought by balanced I/Q down-conversion are also analyzed, which makes the proposed system have better adaptability to different situations. Conclusions are drawn in Section IV.

II. Principle

A. Principle of the Proposed Structure

The schematic diagram of the proposed AOA and frequency measurement system is depicted in Fig. 1(a). A continuous wave (CW) light generated by a laser diode (LD) is equally divided into two branches by an optical coupler (OC), which are used as the optical carriers. The optical carrier in the upper branch is modulated by a single-frequency microwave signal at a dual-parallel Mach-Zehnder Modulator (DPMZM, DPMZM1). The single-frequency signal is generated by a microwave signal generator and connected to two sub-MZMs in DPMZM1 via a 90-degree electrical hybrid. DPMZM1 is biased at carrier-suppressed single sideband (CS-SSB) modulation mode [9] with two sub-MZMs biased at null transmission point and the main MZM biased at quadrature transmission point to achieve an

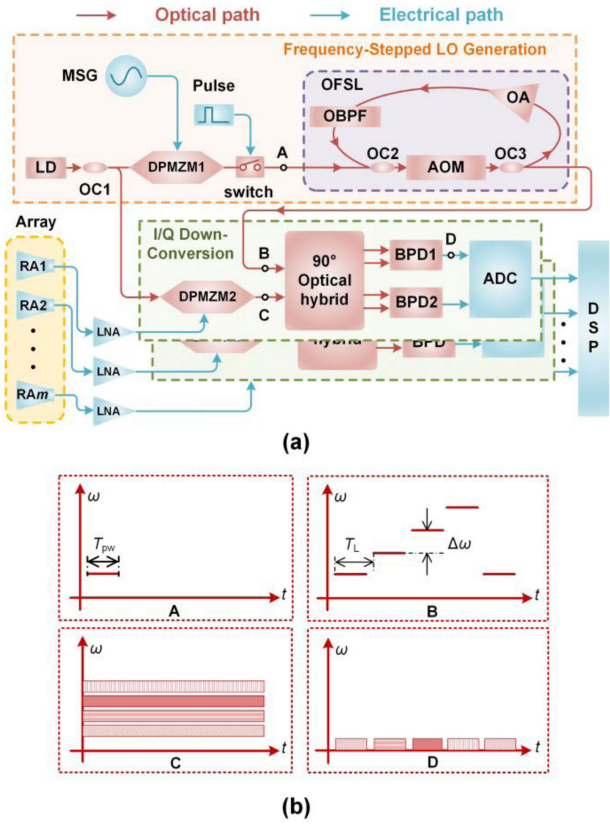

Fig. 1. Schematic diagram of the proposed AOA and frequency measurement system (a) and time-frequency diagram at key points (A-D) in the system (b). LD: laser diode; MSG: microwave signal generator; MZM: Mach-Zehnder modulator; DPMZM: dual parallel MZM; OFSL: optical frequency shift loop; OC: optical coupler; OBPF: optical bandpass filter; AOM: acousto-optic modulator; OA: optical amplifier; RA: received antenna; LNA: low noise amplifier; BPD: balanced photodetector; ADC: analog to digital converter; DSP: digital signal processor.

initial frequency shift. Assuming that the angular frequency of the optical carrier is ω_c, the output of DPMZM1 can be expressed as

$$\begin{aligned} e_{\mathrm{DPMZM}}(t) = &\cos\left(\beta\cos(\omega_0 t) - \frac{\pi}{2}\right)\exp(j\omega_c t) \\ &+ \cos\left(\beta\sin(\omega_0 t) - \frac{\pi}{2}\right)\exp\left(j\omega_c t + j\frac{\pi}{2}\right) \\ &\approx 2J_1(\beta)\exp\left[j(\omega_c + \omega_0)t\right] \end{aligned} \tag{1}$$

where ω_0 and β are the angular frequency and the modulation index of the microwave signal, respectively. $J_1(\cdot)$ is the first-order Bessel function. The output of DPMZM1 is then sent to an optical switch driven by an electrical pulse train to generate a pulse light (Point A), which can be represented as

$$e_{\mathrm{pulse}} = e_0 \cdot \mathrm{rect}\left(\frac{t}{T_{\mathrm{pw}}}\right)\exp\left[j(\omega_c + \omega_0)t\right] \tag{2}$$

Here e_0 is the amplitude of the optical signal, T_{pw} is the pulse duration time. The generated pulse light is then injected into the optical frequency shift loop (OFSL) which consists of an acousto-optic modulator (AOM), an optical amplifier (OA),

Authorized licensed use limited to: NANJING UNIVERSITY OF AERONAUTICS AND ASTRONAUTICS. Downloaded on June 06,2022 at 04:05:33 UTC from IEEE Xplore. Restrictions apply.

and an optical bandpass filter (OBPF). The AOM is used as a single-sideband frequency shifter with a few hundred MHz. The OA is inserted to compensate for the loop loss while the OBPF is added to limit the working bandwidth of the OFSL and suppress the amplified spontaneous emission (ASE) noise. Therefore, an optical frequency-stepped LO is generated at the output of OFSL, including a series of time-division multiplexed frequency channels with a bandwidth of few hundreds of MHz. Assuming that the frequency shift applied by AOM is $\Delta\omega$, the signal at the output of OFSL (Point B) can be written as

$$e_{\mathrm{B}}(t) = \sum_{n=1}^{N} \mathrm{rect}\left(\frac{t - nT_{\mathrm{L}}}{T_{\mathrm{pw}}}\right) \cdot \exp\left[j\left(\omega_{\mathrm{c}} + \omega_0 + n\Delta\omega\right)t + j\varphi_n\right] \tag{3}$$

where T_{L} is the loop delay and φ_n is the extra phase difference introduced by the loop in the nth shift. N is the maximum number of frequency shifts in one period, which is determined by the bandwidth of the OBPF.

In the lower branch, the CW optical carrier is sent to a set of parallel DPMZMs. The RF signals received by the antenna array are upconverted to the optical domain through these DPMZMs. Each antenna is connected to a corresponding modulator via a low noise amplifier (LNA), respectively. The DPMZMs are biased at CS-SSB mode to obtain only the +1st-order sidebands. Assuming that ω_{RF} is the angular frequency of the received RF signal, the output of the mth DPMZM (Point C) can be represented by

$$e_{\mathrm{C}m}(t) \propto J_1(\beta_{\mathrm{RF}}) \exp\left[j\omega_{\mathrm{c}}t + j\omega_{\mathrm{RF}}\left(t - \tau_m\right)\right] \tag{4}$$

where β_{RF} is the modulation index of the received RF signal, and $\tau_m = (m\text{-}1)d\cdot\sin\theta/c$ is the time delay of the RF signal captured by the mth antenna in the uniform linear array (ULA) with the element spacing of d. θ is the AOA to be measured.

Then, the output of the mth DPMZM and the optical frequency-stepped LO are sent to a 90-degree optical hybrid. The four outputs of the optical hybrid can be written as

$$\begin{bmatrix} e_{\mathrm{I}+}(t) \\ e_{\mathrm{I}-}(t) \\ e_{\mathrm{Q}+}(t) \\ e_{\mathrm{Q}-}(t) \end{bmatrix} \propto \begin{bmatrix} 1 & 1 \\ 1 & -1 \\ 1 & j \\ 1 & -j \end{bmatrix} \cdot \begin{bmatrix} e_{\mathrm{B}}(t) \\ e_{\mathrm{C}m}(t) \end{bmatrix} \tag{5}$$

The obtained four optical signals are connected to two balanced photodetectors (BPD) to perform the optical-to-electrical conversion. The outputs of the two BPDs can be expressed as

$$\begin{aligned} \begin{bmatrix} s_{m\mathrm{I}}(t) \\ s_{m\mathrm{Q}}(t) \end{bmatrix} &\propto \begin{bmatrix} |e_{m\mathrm{I}+}(t)|^2 - |e_{m\mathrm{I}-}(t)|^2 \\ |e_{m\mathrm{Q}+}(t)|^2 - |e_{m\mathrm{Q}-}(t)|^2 \end{bmatrix} \\ &\propto \begin{bmatrix} e_{\mathrm{B}}(t)\cdot e^*_{\mathrm{C}m}(t) + e^*_{\mathrm{B}}(t)\cdot e_{\mathrm{C}m}(t) \\ -j\left[e_{\mathrm{B}}(t)\cdot e^*_{\mathrm{C}m}(t) - e^*_{\mathrm{B}}(t)\cdot e_{\mathrm{C}m}(t)\right] \end{bmatrix} \\ &\propto \mathrm{rect}\left(\frac{t - nT_{\mathrm{L}}}{T_{\mathrm{pw}}}\right) \cdot \\ &\quad \begin{bmatrix} \cos\left[\left(\omega_{\mathrm{RF}} - \omega_0 - n\Delta\omega\right)t + \omega_{\mathrm{RF}}\tau_m + \varphi_n\right] \\ -\sin\left[\left(\omega_{\mathrm{RF}} - \omega_0 - n\Delta\omega\right)t + \omega_{\mathrm{RF}}\tau_m + \varphi_n\right] \end{bmatrix} \end{aligned} \tag{6}$$

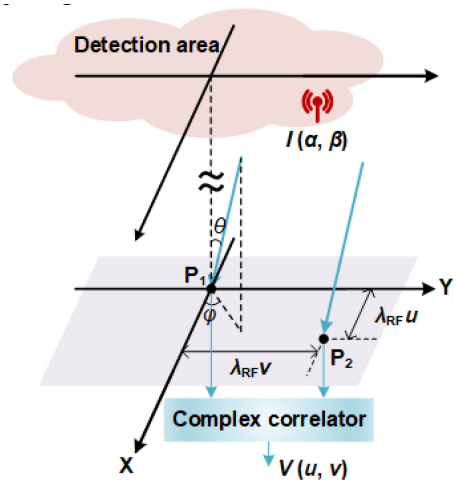

Fig. 2. Geometric position diagram of Van Cittert-Zernike theorem.

As can be seen in (6), two down-converted signals with a phase difference of 90° are generated. Due to the bandwidth limitation of the low-speed BPD, the down-converted low-frequency signal can be output only when the frequency of the RF signal is in the corresponding frequency channel. After analog-to-digital conversion, a complex-valued signal can be synthesized in the digital domain, which can be represented by

$$s_m(t) \propto \mathrm{rect}\left(\frac{t - nT_{\mathrm{L}}}{T_{\mathrm{pw}}}\right) \cdot \exp\left\{j\left[\left(\omega_{\mathrm{RF}} - \omega_0 - n\Delta\omega\right)t + \omega_{\mathrm{RF}}\tau_m - \varphi\right]\right\} \tag{7}$$

By searching the frequency channel where the beat note exists, the shift times n can be derived. Then the frequency of the RF signal can be calculated without ambiguity. The complex-valued signals collected by different antennas are cross-correlated (multiplied and integrated) with each other to obtain the angular domain information.

B. AOA Measurement Principle

The principle used to obtain the AOA of multiple targets is based on Van Cittert-Zernike theorem developed in radio astronomy [31]. The theorem states that when targets with incoherent radiation are in the far-field (or Fraunhofer zone) of the receive array, the Fourier transform of the cross-correlation function between different antennas is equal to the source intensity distribution. Van Cittert-Zernike theorem can be represented by the following formula and the geometric position diagram is depicted in Fig. 2.

$$I(\alpha, \beta) = \iint V(u, v) \exp\left[-j2\pi\left(u\alpha + v\beta\right)\right] du dv \tag{8}$$

where $I(\alpha, \beta)$ is the 2-D spatial scene intensity, $\alpha = \sin\theta\cdot\cos\varphi$, $\beta = \sin\theta\cdot\sin\varphi$ are the direction cosines. Here, θ and φ are spherical coordinates with respect to Cartesian coordinate x and y, respectively. $V(u, v)$ called visibility function is the result of cross-correlation for zero time offset between signals collected by two different elements in the array, where u and v are spatial

Authorized licensed use limited to: NANJING UNIVERSITY OF AERONAUTICS AND ASTRONAUTICS. Downloaded on June 06,2022 at 04:05:33 UTC from IEEE Xplore. Restrictions apply.

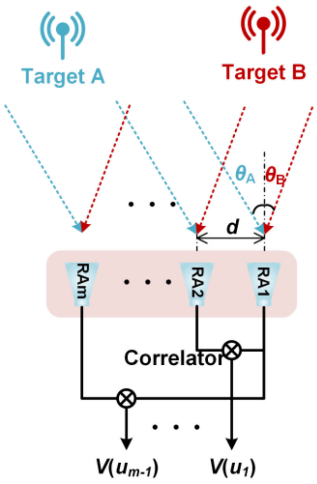

Fig. 3. The schematic diagram of a linear array observing two targets with incoherent radiation.

frequencies corresponding to coordinate x and y, respectively. For an antenna pair $\mathrm{P}_1\,(x_1, y_1)$ and $\mathrm{P}_2\,(x_2, y_2)$ in Fig. 2, the spatial frequencies are given by $u = (x_2\text{-}x_1)/\lambda_{\mathrm{RF}}$, $v = (y_2\text{-}y_1)/\lambda_{\mathrm{RF}}$, here λ_{RF} is the wavelength of the detected RF signal. The theorem indicates that when targets with incoherent radiation are in the far-field of the receive array, the direction of the targets can be derived from the cross-correlation function measured at the receive array.

When the theorem is applied to the proposed AOA measurement system with a 1-D linear array as shown in Fig. 3, the 2-D Fourier transform can be simplified to the 1-D Fourier transform. In addition, since the coordinates of array elements in the practical array are discrete values, the Fourier transform should be written in discrete form.

$$I\left(\alpha\right) = \sum_{m} V\left(u_m\right) \exp\left(-j2\pi u_m \alpha\right) \tag{9}$$

Here, $I(\alpha)$ is 1-D spatial scene intensity containing the angular domain information. $V(u_m)$ is the cross-correlation result for zero time offset between the signals collected by the 1st and the m+1th channel, which corresponds to a specific spatial frequency u_m and can be expressed as

$$\begin{aligned} V\left(u_m\right) &= \left\langle s_1\left(t\right) \cdot s_{m+1}^{*}\left(t\right)\right\rangle \\ &\propto \left\langle \mathrm{rect}^2\left(t - nT_{\mathrm{L}}/T_{pw}\right)\right. \\ &\quad \cdot \exp\left\{j\left[\left(\omega_{\mathrm{RF}} - n\Delta\omega\right)t + \omega_{\mathrm{RF}}\tau_1\right]\right\} \\ &\quad \left.\cdot \exp\left\{-j\left[\left(\omega_{\mathrm{RF}} - n\Delta\omega\right)t + \omega_{\mathrm{RF}}\tau_{m+1}\right]\right\}\right\rangle \\ &\propto \int \exp\left(j\omega_{\mathrm{RF}}\Delta\tau_m\right)dt \\ &\propto \exp\left(j2\pi d_m/\lambda_{\mathrm{RF}} \cdot \sin\theta\right) \end{aligned} \tag{10}$$

where $<\cdot>$ represents a time average operation, $\Delta\tau_m$ is the time delay difference between the selected two antenna elements, d_m is the length of the mth baseline (separation between the 1st and the m+1th antenna in the linear array). By collecting the cross-correlation result corresponding to different spatial frequencies (or baselines) and fusing them through inverse Fourier transform, the spatial scene intensity will be obtained [32].

In practical applications, multiple targets often appear at the same time. Therefore, it is necessary to analyze the capability of multiple-target detection. Consider a two targets detection scenario depicted in Fig. 3, the cross-correlation can be represented by

$$\begin{aligned} V_{\mathrm{A+B}}\left(u_m\right) &= \left\langle s_1\left(t\right) \cdot s_2\left(t\right)\right\rangle \\ &= \left\langle \left(s_{1\mathrm{A}}\left(t\right) + s_{1\mathrm{B}}\left(t\right)\right) \cdot \left(s_{2\mathrm{A}}\left(t\right) + s_{2\mathrm{B}}\left(t\right)\right)\right\rangle \\ &\approx \left\langle s_{1\mathrm{A}}\left(t\right) \cdot s_{2\mathrm{A}}\left(t\right)\right\rangle + \left\langle s_{1\mathrm{B}}\left(t\right) \cdot s_{2\mathrm{B}}\left(t\right)\right\rangle \end{aligned} \tag{11}$$

where $s_{m\mathrm{A}}(t)$, and $s_{\mathrm{mB}}(t)$ are signals emitted by target A and B, respectively, which are collected by the mth antenna element. Due to the incoherent radiation assumption mentioned above, the coherence between signals from different targets is very low. Therefore, the cross-correlation term between different targets can be ignored, and only the common parts are retained. The dual-target visibility function can then be simplified into a sum of two single-target visibility functions. Furthermore, according to the linear properties of the Fourier transform, the dual-target far-field intensity can be expressed as the superposition of the two targets.

$$\begin{aligned} I_{\mathrm{A+B}}\left(\alpha\right) &= F^{-1}\left(V_{\mathrm{A}}\left(u_m\right) + V_{\mathrm{B}}\left(u_m\right)\right) \\ &= F^{-1}\left(V_{\mathrm{A}}\left(u_m\right)\right) + F^{-1}\left(V_{\mathrm{B}}\left(u_m\right)\right) \\ &= I_{\mathrm{A}}\left(\alpha\right) + I_{\mathrm{B}}\left(\alpha\right) \end{aligned} \tag{12}$$

Thus, when the electromagnetic radiation from different targets is incoherent, multiple-target detection can be achieved.

III. Experiments and Results

A proof-of-concept experiment is carried out based on the schematic diagram in Fig. 1. A CW optical carrier at 193.4 THz is generated by an LD and divided into two branches through a 50:50 OC. In the upper branch, the optical carrier is directed to a DPMZM (Fujitsu FTM7961). A microwave signal generator (R&S SMA100B) is implemented to generate a pulsed-modulated single-frequency microwave signal with a frequency of 7.8 GHz, a pulse width of 5 μs, and a period of 600 μs. The generated microwave signal is then split by a 90-degree electrical hybrid for CS-SSB modulation at the DPMZM. Since the driving signal of the DPMZM is a pulsed-modulated signal, the DPMZM is used as an optical switch and a frequency shifter at the same time. The optical spectrum after DPMZM (Point A) is shown in Fig. 4 by the solid curve. The spectrum is measured by an optical spectrum analyzer (Yokogawa AQ6370C). The output of the DPMZM is then sent into the OFSL, which is composed of an AOM with a bandwidth of 200 MHz, an erbium-doped fiber amplifier (EDFA, Amonics AEDFA-PA-35B), a span of 1-km fiber, an OBPF (Yenista XTM-50 Ultrafine), and a 50:50 2×2 OC. The optical frequency-stepped LO with a frequency interval of 200 MHz is then generated after carefully tuning the input power of OFSL and the gain of EDFA. The output spectrum from the OFSL (Point B) is depicted in Fig. 4 by the

Authorized licensed use limited to: NANJING UNIVERSITY OF AERONAUTICS AND ASTRONAUTICS. Downloaded on June 06,2022 at 04:05:33 UTC from IEEE Xplore. Restrictions apply.

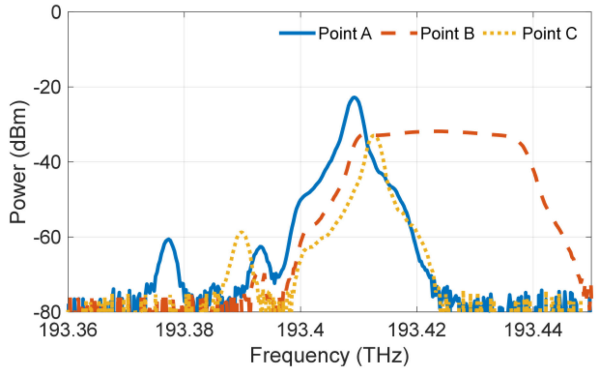

Fig. 4. Optical spectra at several key points in the proposed system. Solid blue line: output of the DPMZM in the upper branch (Point A), dashed orange line: output of OFSL (Point B), dotted yellow line: output of PDM-DPMZM in the lower branch (Point C).

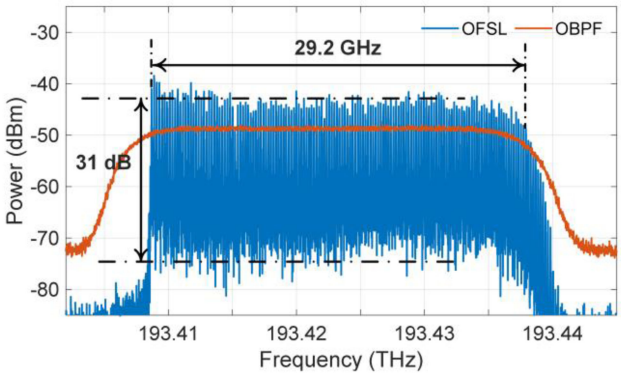

Fig. 5. Frequency response of OFSL (blue line) and OBPF (orange line) captured by the high-resolution optical spectrum analyzer.

dashed curve. The optical spectrum at point B measured by a high-resolution optical spectrum analyzer is shown in Fig. 5 by the solid blue line. The signal-to-noise ratio inside the passband of the OBPF is about 31 dB. The total 3-dB bandwidth of the frequency-stepped LO is about 29.2 GHz.

The CW optical carrier in the lower branch is sent to a polarization-division-multiplexed DPMZM (PDM-DPMZM, Fujitsu FTM7977) which has a sub-DPMZM in the X and Y polarization respectively. Signals collected by two elements in the array are sent to two sub-DPMZMs. Both sub-DPMZMs are biased at CS-SSB mode. The optical spectrum after PDM-DPMZM (Point C) is presented in Fig. 4 by dotted curve.

The output of the PDM-DPMZM is connected to a dual-polarization 90-degree optical hybrid via a polarization controller (PC). By properly adjusting the PC, the signals of two sub-DPMZMs can be separated. Two low-speed BPDs (Thorlabs PDB450C-AC, bandwidth 150 MHz) are then applied after the optical hybrid to achieve optical-to-electro conversion. The generated low-frequency electrical signal is sampled by a real-time oscilloscope with a sampling rate of 200 MSa/s.

What needs to be noted here is that under ideal conditions, the AOA should be measured by collecting signals of all elements in the linear array simultaneously. However, due to the hardware

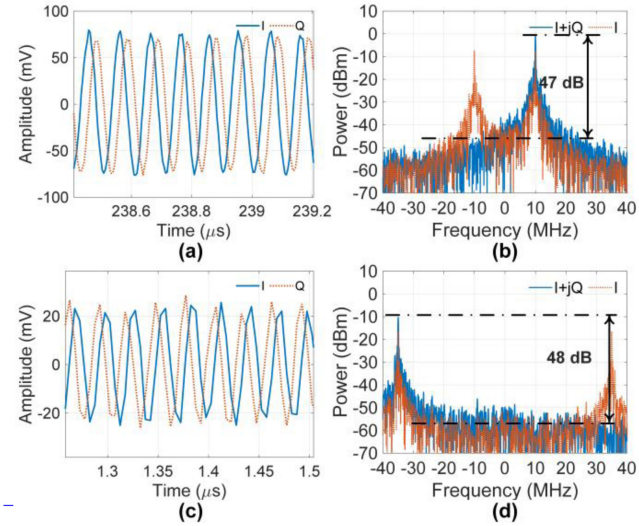

Fig. 6. The time domain waveform of down-converted signal at 10.21 GHz (a) and 11.165 GHz (c), corresponding spectra of I channel and the synthesized complex-valued signal (b) (d).

limitation, only two channels of signals can be captured at the same time, and the AOA is measured by selecting two elements with different separations in the array to synthesize an equivalent 1-D aperture. Therefore, the PDM-DPMZM and dual-polarization 90-degree optical hybrid applied in the experiment are used to provide two identical I/Q down-conversion links.

A. *Frequency Measurement*

To investigate the performance of the proposed system, frequency measurement experiment is first carried out. A single-frequency signal at 10.21 GHz generated by a microwave signal generator is used as a detected signal. The waveform of down-converted signal and corresponding frequency spectrum is shown in Fig. 6(a) and (b). The frequency of the down-converted signal is 10 MHz. Since 10.21 GHz is in the channel around 10.20 GHz and is higher than the reference frequency, the frequency of the obtained complex-valued signal is positive, which is represented by the solid blue line in Fig. 6(b). After I/Q imbalance compensation according to [33], the image-rejection ratio is about 47 dB. Another single-frequency signal at 11.165 GHz is also applied, which is lower than the reference frequency 11.20 GHz. The frequency of the obtained complex-valued signal is −35 MHz. The corresponding spectrum is shown in Fig. 6(d), where a 48-dB image-rejection ratio is achieved.

Then, to manifest the ability of multiple-target detection, measurement of multiple frequencies is performed. A two-tone signal at 11.02 GHz and 11.03 GHz is generated as the target signal. The frequency spectra of down-converted signals obtained by single-end PD (SPD) and BPD are presented in Fig. 7. As can be seen in the spectra obtained by SPD, which is presented by dotted orange line, three frequency components are generated. Two spectral peaks at 20 MHz and 30 MHz are the down-converted target signals according to the reference frequency of 11 GHz.

Authorized licensed use limited to: NANJING UNIVERSITY OF AERONAUTICS AND ASTRONAUTICS. Downloaded on June 06,2022 at 04:05:33 UTC from IEEE Xplore. Restrictions apply.

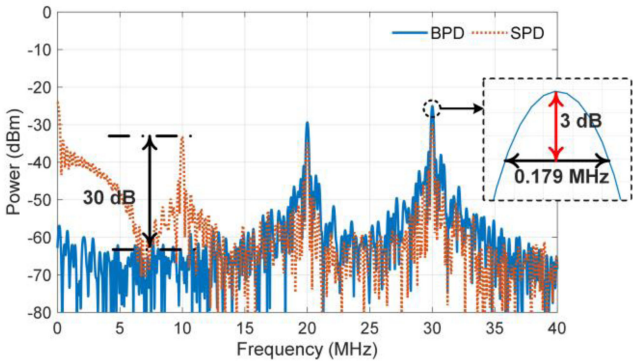

Fig. 7. The spectra of down-converted signals obtained by single-end PD (SPD, dotted orange line) and BPD (solid blue line) when a two-tone signal is tested.

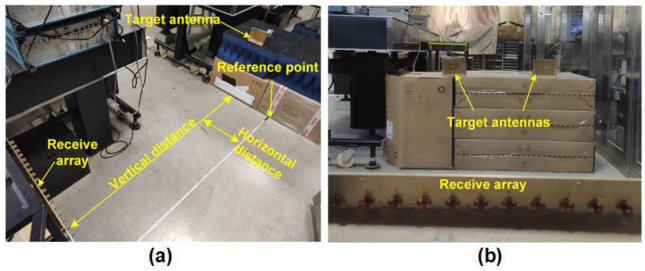

Fig. 8. Experiment setup of AOA measurement (a) and picture of dual-target detection (b).

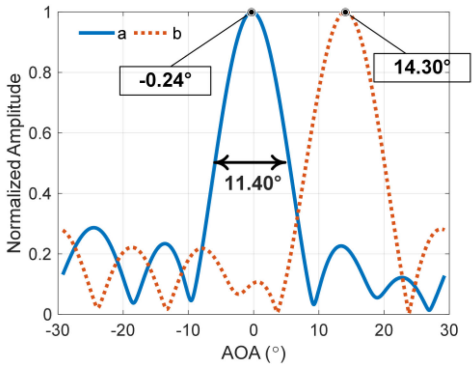

Fig. 9. The obtained single target AOA measurement results. Target antenna at 0° (solid blue line, a) and 14.04° (dotted orange line, b).

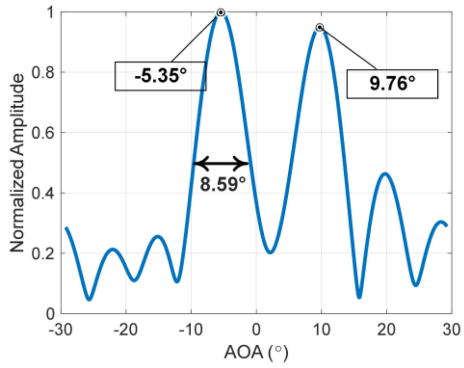

Fig. 10. The obtained dual-target AOA measurement result.

In addition, an undesired frequency component at 10 MHz is relatively high, which is generated due to the frequency mixing between the two original frequencies. By applying balanced detection, the undesired frequency component can be greatly suppressed. The suppression ratio is about 30 dB compared with the spectra obtained by SPD. Furthermore, the baseband components around zero frequency are also significantly suppressed. This capability is quite important when dealing with multiple targets. The frequency measurement resolution is also tested. As is shown in the zoom-in view of the spectra in Fig. 7, the 3-dB bandwidth is 0.179 MHz, which is very close to the theoretical resolution of 0.178 MHz corresponding to the duration of 5 μs [34].

B. AOA Measurement

In the AOA measurement experiment, two horn antennas are used as target sources. An X-band ULA with antenna elements interval of 3 cm is used as the receive array. The experiment setup is depicted in Fig. 8(a), where the vertical distance between the plane of the target antennas and the ULA is 1.8 m. To calculate the theoretical AOA, the target antennas are placed at different horizontal distances from the reference point where AOA is 0°. The theoretical AOA is calculated according to the horizontal distances and the vertical distance. Without losing generality, we assume that the AOA of the antenna on the right side of the reference point is positive.

Single target AOA measurement is first carried out. The target antenna is first placed at the reference point. To simulate a practical scenario, a band-limited gauss noise signal with a center frequency of 10.23 GHz and a bandwidth of 40 MHz is used as the transmitted signal. The measurement result is shown in Fig. 9 in solid blue line (a), where the measured AOA is -0.24°. Then the target antenna is placed at a horizontal distance of 45 cm to the right of the reference point. It can be calculated that the theoretical AOA is 14.04°. The measurement result is shown in Fig. 9 by dotted orange line (b), showing that the measured AOA is 14.30°.

Then, dual-target AOA measurement is conducted based on the setup in Fig. 8(b). Two target antennas are placed on different sides of the reference point. Antenna 1 is placed 15 cm to the left of the reference point, and antenna 2 is placed 30 cm to the right of the reference point. The theoretical AOAs can be calculated as $-4.76°$ and 9.46°, respectively. The transmitted signals of the two antennas are incoherent gauss noise signals with the same frequency band (10.21$\sim$10.25 GHz). The obtained measurement result is depicted in Fig. 10. As can be seen, the two target sources with the same frequency band but different AOAs can be distinguished clearly. The measured AOAs are $-5.35°$ and 9.76°, respectively.

In the dual-target AOA measurement, data received by 9 elements are collected. The theoretical resolution should be $0.89\lambda/(\pi D)\cdot 180° = 6.22°$. However, the 3-dB bandwidth of

Authorized licensed use limited to: NANJING UNIVERSITY OF AERONAUTICS AND ASTRONAUTICS. Downloaded on June 06,2022 at 04:05:33 UTC from IEEE Xplore. Restrictions apply.

the obtained result in Fig. 10 is about 8.59°, with considerable deterioration. Similar deterioration also occurs in single target detection using 7 elements, in which the resolution is deteriorating from 8.30° to 11.40°.

Here, the AOA measurement error and resolution deterioration in the experiment can be summarized into three reasons. Firstly, the far-field assumption is not fully satisfied. Due to the limitation of experiment conditions, the detection range is relatively short. Therefore, the amplitude of signals received by each element is not equal, which causes the widening of the main lobe. Secondly, the size of the X-band horn antennas used in the experiment is quite large (10.6 cm×13.7 cm) compared with the detection range, which cannot be completely equivalent to an ideal point target. Thirdly, the point spread function (PSF) of the array and the impact of the transfer functions of the devices used in the system are not considered in Van Cittert-Zernike theorem, which will also distort the AOA measurement results [35].

Although only narrowband signals are tested in the experiment, the AOA of wideband signals can also be measured due to the large working bandwidth. It is also worth noting that the proposed system can characterize the intensity of the target source as well as the AOA. Therefore, it can be further extended to a passive 2-D imaging system by applying a 2-D array [30]. In addition, a sparse array or compressive coding algorithm can be applied to reduce the hardware complexity of the system [35], [36]. We are planning to carry out the related research in future work.

IV. Discussion and Conclusion

In the experiment, limited by the operation bandwidth of the X-band antennas of the array, the frequency coverage of the established system is about 8∼12 GHz. If a wideband antenna array is applied, the operating frequency range of can be enlarged to up to 30 GHz, which is determined by the bandwidth of the OFSL response. It should also be noted that, although the measurement of two frequencies are demonstrated, the frequency measurement error is theoretically independent of the frequency to be measured, since the frequency measurement is acquired through broadband down-conversion and digital signal processing. The AOA measurement error can be evaluated by the Cramer-Rao Lower Bound (CRLB) [37].

$$\mathrm{VAR}\left(\hat{\theta}\right) \geq \frac{6}{L\left(L^2-1\right)\mathrm{SNR}k^2d^2\cos^2\left(\theta\right)} \tag{13}$$

where $\hat{\theta}$ is the estimated AOA, $VAR(\hat{\theta})$ is the variance of the AOA estimation, L is the number of antennas in the linear array, SNR is the signal-to-noise ratio of the system, k is the wavenumber of the incoming signal, d is the distance between two adjacent antennas. Thus, the error of AOA estimation is dependent on the frequency and the direction of the incoming signal. When the size of the antenna array (L and d) and SNR are fixed, the AOA measurement error becomes smaller as the signal frequency increases, and it becomes larger as the incident angle of the signal becomes larger.

In conclusion, we have proposed and experimentally demonstrated a photonics-based simultaneous angle of arrival and frequency measurement system for multiple-target detection. By combining the optical time-division channelized I/Q down-conversion and the array signal processing method based on Van Cittert-Zernike theorem, frequencies and AOA of multiple targets can be measured simultaneously. In the experiment, target antennas with different frequencies and AOAs are detected to verify the feasibility of the proposed system. Compared to the previously reported photonics-based AOA measurement system, the proposed system can be applied in multiple-target scenarios, which provides a novel solution for photonics-based passive detection systems.

References

[1] M. Khan, N. Salman, and A. Kemp, "Cooperative positioning using angle of arrival and time of arrival," in *Proc. IEEE Sensor Signal Process. Defence*, 2014, pp. 1–5.

[2] B. Zong, C. Fan, X. Wang, X. Duan, B. Wang, and J. Wang, "6G technologies: Key drivers, core requirements, system architectures, and enabling technologies," *IEEE Veh. Technol. Mag.*, vol. 14, no. 3, pp. 18–27, Sep. 2019.

[3] A. E. Spezio, "Electronic warfare systems," *IEEE Trans. Microw. Theory Techn.*, vol. 50, no. 3, pp. 633–644, Mar. 2002.

[4] J. Yao, "Microwave photonics," *J. Lightw. Technol.*, vol. 27, no. 1-4, pp. 314–335, Feb. 2009.

[5] S. Pan and Y. Zhang, "Microwave photonic radars," *J. Lightw. Technol.*, vol. 38, no. 19, pp. 5450–5484, Oct. 2020.

[6] X. Zou, B. Lu, W. Pan, L. Yan, A. Stöhr, and J. Yao, "Photonics for microwave measurements," *Laser Photon. Rev.*, vol. 10, no. 5, pp. 711–734, Sep. 2016.

[7] S. Pan and J. Yao, "Photonics-based broadband microwave measurement," *J. Lightw. Technol.*, vol. 35, no. 16, pp. 3498–3513, Aug. 2017.

[8] P. Ghelfi *et al.*, "A fully photonics-based coherent radar system," *Nature*, vol. 507, no. 7492, pp. 341–345, Mar. 2014.

[9] C. Ma *et al.*, "Microwave photonic imaging radar with a sub-centimeter-level resolution," *J. Lightw. Technol.*, vol. 38, no. 18, pp. 4948–4954, Sep. 2020.

[10] Z. Tang, Y. Li, J. Yao, and S. Pan, "Photonics-based microwave frequency mixing: Methodology and applications," *Laser Photon. Rev.*, vol. 14, no. 1, Jan. 2020, Art. no. 1800350.

[11] X. Ye, F. Zhang, Y. Yang, and S. Pan, "Photonics-based radar with balanced I/Q de-chirping for interference-suppressed high-resolution detection and imaging," *Photon. Res.*, vol. 27, no. 3, pp. 265–272, Mar. 2019.

[12] S. Pan, X. Ye, Y. Zhang, and F. Zhang, "Microwave photonic array radars," *IEEE J. Microw.*, vol. 1, no. 1, pp. 176–190, Winter 2021.

[13] F. Zhang *et al.*., "Photonics-based broadband radar for high-resolution and real-time inverse synthetic aperture imaging," *Opt. Exp.*, vol. 25, no. 14, pp. 16274–16281, Jul. 2017.

[14] F. Zhang *et al.*, "Photonics-based MIMO radar with high-resolution and fast detection capability," *Opt. Exp.*, vol. 26, no. 14, pp. 17529–17540, Jun. 2018.

[15] B. Vidal, M. A. Piqueras, and J. Marti, "Direction-of-arrival estimation of broadband microwave signals in phased-array antennas using photonic techniques," *J. Lightw. Technol.*, vol. 24, no. 7, pp. 2741–2745, Jul. 2006.

[16] X. Zou, W. Li, W. Pan, B. Luo, L. Yan, and J. Yao, "Photonic approach to the measurement of time-difference-of-arrival and angle-of-arrival of a microwave signal," *Opt. Lett.*, vol. 37, no. 4, pp. 755–757, Feb. 2012.

[17] Z. Cao, H. P. A. van den Boom, R. Lu, Q. Wang, E. Tangdiongga, and A. M. J. Koonen, "Angle-of-arrival measurement of a microwave signal using parallel optical delay detector," *IEEE Photon. Technol. Lett.*, vol. 25, no. 19, pp. 1932–1935, Oct. 2013.

[18] H. Chen and E. H. W. Chan, "Angle-of-arrival measurement system using double RF modulation technique," *IEEE Photon. J.*, vol. 11, no. 1, Feb. 2019, Art. no. 7200110.

[19] H. Chen and E. H. W. Chan, "Simple approach to measure angle of arrival of a microwave signal," *IEEE Photon. Technol. Lett.*, vol. 31, no. 22, pp. 1795–1798, Nov. 2019.

Authorized licensed use limited to: NANJING UNIVERSITY OF AERONAUTICS AND ASTRONAUTICS. Downloaded on June 06,2022 at 04:05:33 UTC from IEEE Xplore. Restrictions apply.

[20] H. Chen and E. H. W. Chan, "Photonics-based CW/Pulsed microwave signal AOA measurement system," *J. Lightw. Technol.*, vol. 38, no. 8, pp. 2292–2298, Apr. 2020.
[21] P. Li *et al.*, "Angle-of-arrival estimation of microwave signals based on optical phase scanning," *J. Lightw. Technol.*, vol. 37, no. 24, pp. 6048–6053, Dec. 2019.
[22] S. Li, H. Cao, and X. Zheng, "Concurrent photonic measurement of angle-of-arrival and chirp rate of microwave LFM signal," *Chin. Opt. Lett.*, vol. 18, no. 12, Dec. 2020, Art. no. 123902.
[23] H. Chen, C. Huang, and E. H. W. Chan, "Photonic approach for measuring AOA of multiple signals with improved measurement accuracy," *IEEE Photon. J.*, vol. 12, no. 3, pp. 1–10, Jun. 2020.
[24] Z. Tang and S. Pan, "Simultaneous measurement of Doppler-frequency-shift and angle-of-arrival of microwave signals for automotive radars," in *Proc. Int. Top. Meeting Microw. Photon.*, 2019, pp. 1–4.
[25] R. Toole and M. P. Fok, "Photonic implementation of a neuronal algorithm applicable towards angle of arrival detection and localization," *Opt. Exp.*, vol. 23, no. 12, pp. 16133–16141, Jun. 2015.
[26] J. Murakowski, G. J. Schneider, S. Shi, C. A. Schuetz, and D. W. Prather, "Photonic probing of radio waves for k-space tomography," *Opt. Exp.*, vol. 25, no. 14, pp. 15746–15759, Jul. 2017.
[27] D. D. Ross, C. J. Ryan, G. J. Schneider, J. Murakowski, and D. W. Prather, "Passive three-dimensional spatial-spectral analysis based on k-space tomography," *IEEE Photon. Technol. Lett.*, vol. 30, no. 9, pp. 817–820, May 2018.
[28] C. J. Ryan, D. D. Ross, J. Murakowski, G. J. Schneider, and D. W. Prather, "Kalman-filter accelerated k-space tomography," *J. Lightw. Technol.*, vol. 37, no. 3, pp. 942–948, Feb. 2019.
[29] Y. Yang, C. Ma, F. Zhang, B. Fan, X. Wang, and S. Pan, "Photonics-based simultaneous angle of arrival and frequency measurement for multiple targets detection," in *Proc. Int. Top. Meeting Microw. Photon.*, 2020, pp. 14–17.
[30] S. Vakalis, L. Gong, Y. He, J. Papapolymerou, and J. A. Nanzer, "Experimental demonstration and calibration of a 16-element active incoherent millimeter-wave imaging array," *IEEE Trans. Microw. Theory Techn.*, vol. 68, no. 9, pp. 3804–3813, Sep. 2020.
[31] A. R. Thompson, J. M. Moran, and G. W. Swenson, Jr, *Interferometry and Synthesis in Radio Astronomy*. Cham, Switzerland: Springer Nature, 2017.
[32] J. A. Nanzer, S. Vakalis, L. Gong, Y. He, and J. Papapolymerou, "Incoherent imaging at microwave and millimeter-wave frequencies using noise transmitters," *IEEE Aerosp. Electron. Syst. Mag.*, vol. 35, no. 10, pp. 42–51, Oct. 2020.
[33] M. A. Richards, "Pulsed radar data acquisition," in *Fundamentals of Radar Signal Processing*. NY, USA: McGraw-Hill, 2014, pp. 183–229.
[34] M. Henri, "The principles of synthetic aperture radar," in *Processing of Synthetic Aperture Radar Images*. London, U.K.: ISTE Ltd, John Wiley Sons, 2008, pp. 25–55.
[35] E. Kpre, C. Decroze, M. Mouhamadou, and T. Fromenteze, "Computational imaging for compressive synthetic aperture interferometric radiometer," *IEEE Trans. Antennas Propag.*, vol. 66, no. 10, pp. 5546–5557, Oct. 2018.
[36] S. Vakalis and J. A. Nanzer, "Analysis of array sparsity in active incoherent microwave imaging," *IEEE Geosci. Remote Sens. Lett.*, vol. 17, no. 1, pp. 57–61, Jan. 2020.
[37] S. Sand, A. Dammann, and C. Mensing, "Measurements and parameter extraction," in *Positioning in Wireless Communications Systems*. NJ, USA: John Wiley Sons, 2014, pp. 41–68.

Authorized licensed use limited to: NANJING UNIVERSITY OF AERONAUTICS AND ASTRONAUTICS. Downloaded on June 06,2022 at 04:05:33 UTC from IEEE Xplore. Restrictions apply.